Pedestrian Imaging Using UWB Doppler Radar Interferometry

Kenshi SAHO[†a)], *Student Member*, Takuya SAKAMOTO[†], *Member*, Toru SATO[†], *Fellow*, Kenichi INOUE[††], *and* Takeshi FUKUDA[††], *Members*

SUMMARY The imaging of humans using radar is promising for surveillance systems. Although conventional radar systems detect the presence or position of intruders, it is difficult to acquire shape and motion details because the resolution is insufficient. This paper presents a high-resolution human imaging algorithm for an ultra-wideband (UWB) Doppler radar. The proposed algorithm estimates three-dimensional human images using interferometry and, using velocity information, rejects false images created by the interference of body parts. Experiments verify that our proposed algorithm achieves adequate pedestrian imaging. In addition, accurate shape and motion parameters are extracted from the estimated images.

key words: *human imaging, pedestrian imaging, UWB Doppler radar, interferometry, false image rejection*

1. Introduction

Surveillance systems have become increasingly prevalent in society. A key goal for these systems is accurate imaging of the human body. Although cameras have been used for such applications, their sensitivity in low-light conditions and their range resolution are inadequate [1], [2]. High-resolution imaging methods with multiple cameras have also been proposed [3]–[5]. However, the system size becomes too large because of the numerous cameras required.

To overcome these problems, radar systems have been studied and applied to the detection of intruders [6]–[9]. However, these systems are only able to estimate position to the order of 10 cm and are unable to provide shape information. To estimate the shape estimation of moving targets, inverse synthetic aperture radar systems have been proposed [10], [11], but they are computationally time-consuming and provide inadequate resolution. As a solution to these problems, ultra-wideband (UWB) radar is an efficient tool because of its high-resolution capability [12]. A shape estimation algorithm using UWB radar for a moving target has been proposed and has achieved high-resolution imaging with a small number of fixed antennas [13], [14]. However, because this algorithm considers only simple convex targets, applying it to complex targets such as the human body is difficult.

To detect moving bodies, Lin and Ling [15]–[17] proposed an interferometric imaging algorithm with continuous wave (CW) Doppler radar. This algorithm separates multiple targets using the differences in their Doppler frequencies and extracts the direction of arrival (DOA) of each target using interferometry techniques. In [16], this algorithm achieved frontal imaging of a human. However, the range resolution was inadequate because it used CW radar. In addition, spurious images were detected owing to interference from the body parts. Therefore, this algorithm cannot acquire the details of the shape and motion information of moving humans. For the acquisition of motion information, Kim and Ling [18] proposed a motion classification method with a spectrogram obtained by CW Doppler radar. However, this method only estimates motion types (walking, running, sitting, and so on) and cannot estimate motion parameters.

This paper presents a human imaging algorithm with UWB Doppler radar and an application example through experiments. First, we explain a basic UWB Doppler radar interferometric imaging algorithm with a range interpolation method. We examine the experimental examples with this algorithm and show that many false images are estimated owing to interference from body parts. To resolve this problem, we introduce two false image detection and rejection methods that use velocity information. Our experiment assumes a pedestrian and shows that many false images are rejected by the proposed methods. The proposed imaging algorithm achieves adequate human imaging in a real environment, and extracts accurate shape and motion parameters from the estimated human image. Finally, we also show the imaging examples of pedestrians walking in various directions.

2. System Model

Figure 1 shows the system model. We assume that the target is a pedestrian. A transmitting antenna Tx and receiving antennas Rx_1, $_2$, and $_3$ are set up in the $x - z$ plane, and an interferometer is configured using the receiving antennas. The positions of antennas Tx, Rx_1, Rx_2, and Rx_3 are expressed as $(x, z) = (d/2, d/2+z_c)$, $(-d/2, -d/2+z_c)$, $(d/2, -d/2+z_c)$ and $(-d/2, d/2+z_c)$. The pair of receiving antennas Rx_1 and Rx_2 constitutes a horizontal interferometer and the pair of Rx_1 and Rx_3 constitutes a vertical interferometer. A setting of the antenna separation d is discussed in Sect. 4. We take
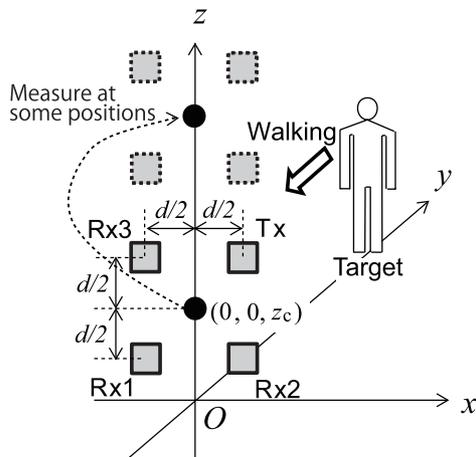
Fig. 1 System model.

measurements at some z_c, and an image is acquired by a superposition of imaging result at each position z_c. The transmitting signal $s_T(t)$ is a UWB signal with a center frequency f_0. The bandwidth is W, which corresponds to a downrange resolution of $\Delta R = c/2W$, where c is the speed of light. We acquire received signal $s_{ik}(t)$ in range bin k using each Rx_i.

3. Basic UWB Doppler Radar Interferometric Imaging Algorithm

The UWB Doppler radar interferometric imaging algorithm separates multiple targets in the frequency domain and estimates the scattering center position of each target using interferometry [15], [16] and a range interpolation method. If different moving targets have different radial velocities, we can separate these targets by the differences in their Doppler frequencies. Since human body parts such as arms and legs generally have different motions, we regard them as multiple moving targets. The Doppler frequency of target n is expressed as:

$$f_{dn} = \frac{2v_{dn}}{\lambda}, \qquad (1)$$

where v_{dn} is the radial velocity of the target n and λ is the wavelength.

To detect f_{dn}, we determine the time-frequency distribution of the received signals. A transmitting signal $s_T(t)$ is expressed as:

$$s_T(t) = T(t)e^{j2\pi f_0 t}, \qquad (2)$$

where $j = \sqrt{-1}$ and $T(t)$ is the transmitting waveform. The received signal at Rx_i is expressed as:

$$s_i(t) = e^{-j2\pi f_0 t} \sum_n \alpha_{Rn} s_T(t - \tau_{pn})e^{j2\pi f_{dn}(t - \tau_{pn})}, \qquad (3)$$

where τ_{pn} is the time delay corresponding to the distance between the Rx_i and the target n, and $\alpha_{Rn} = A_{Rn}/A < 1$ is the ratio of a receiving amplitude A_{Rn} to a transmitting amplitude A. We acquire $s_{ik}(t)$ by a discretization of $s_i(t)$ in terms

of the time delay. The time delay after the discretization corresponding to range bin k is expressed as $\tau_{pk} = 2k\Delta R/c$. The time-frequency distributions of received signals are then calculated for the scattering center separation. In this study, the time-frequency distribution $S_{ik}(t, v_d)$ is obtained by a sliding-window discrete Fourier transform (SDFT) [19] of $s_{ik}(t)$. $S_{ik}(t, v_d)$ is calculated by:

$$S_{ik}(t, v_d) = \int_{-\infty}^{\infty} s_{ik}(\tau)w_H(\tau - t)e^{-j4\pi\tau v_d/\lambda}d\tau, \qquad (4)$$

where $w_H(t)$ is the hamming window function, which is expressed as:

$$w_H(t) = \begin{cases} 0.54 - 0.46\cos\dfrac{2\pi}{T_w}t & (0 \leqq t \leqq T_w) \\ 0 & (\text{otherwise}), \end{cases} \qquad (5)$$

where T_w is the window size. The SDFT calculates Eq. (4) at all time bins. We extract the peaks corresponding to the scattering centers from the time-frequency distribution. Significant peaks of $S_{ik}(t, v_d)$ are extracted using the following conditions:

$$d|S_{ik}(t, v_d)|/dv_d = 0, \qquad (6)$$

$$|S_{ik}(t, v_d)|^2 > \rho \max_{t, v_d} |S_{ik}(t, v_d)|^2, \qquad (7)$$

where $\rho > 0$ is the ratio of the peak extraction threshold power to the maximum power, and is empirically determined.

The scattering centers of each separated target are then estimated by mapping its $t - v_d$ on a plane of distance and DOA, which is determined by the interferometry. The elevation DOA θ_{ELn} and azimuth DOA θ_{AZn} of target n are calculated as:

$$\theta_{ELn}(t) = \sin^{-1}\left[\frac{\angle S_{1k'}(t, v_{dn}) - \angle S_{3k'}(t, v_{dn})}{(2\pi d/\lambda)}\right], \qquad (8)$$

$$\theta_{AZn}(t) = \sin^{-1}\left[\frac{\angle S_{1k'}(t, v_{dn}) - \angle S_{2k'}(t, v_{dn})}{(2\pi d\cos\theta_{ELn}(t)/\lambda)}\right], \qquad (9)$$

where k' is the range bin where target n is detected.

The distance $R_1(t, v_{dn})$ is estimated by finding the range that maximizes the echo intensity as:

$$R_1(t, v_{dn}) = \Delta R \arg\max_k |S_{1k}(t, v_{dn})|. \qquad (10)$$

To realize high-resolution imaging, however, we must estimate the distance to an accuracy that is better than the range resolution because our system assumes that ΔR is of the order of 10 cm. This resolution is insufficient for human shape estimation. For this purpose, the proposed algorithm uses an interpolation between the range gates based on the echo power ratio round the peak. Figure 2 shows an example of the received signal and true range $R(t, v_{dn})$. We estimate $R(t, v_{dn})$ using the fractional range $D(\rho_p)$ determined by a calibration experiment. We first performed the calibration experiment, in which the echo power ratio was measured at the two adjacent range gates around the peak when the fractional range D ($0 \leq D < \Delta R$) of a point target was varied.
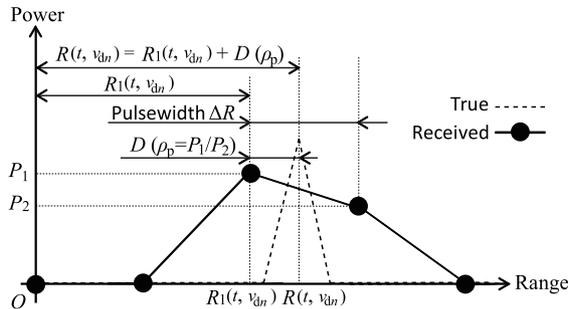
Fig. 2 Example of received signal and the relationship between the true range $R(t, v_{dn})$ and the fractional range $D(\rho_p)$.

Fig. 3 Experimental site of the target on the treadmill.

Fig. 4 Outline of relationship between target and illumination area of transmission beam.

In this calibration experiment, we measure the maximum power P_1 of the received signal, and the power P_2, which is the larger value of the adjacent powers of the maximum power point. Then, the echo power ratio $\rho_p(D)$ is defined as:

$$\rho_p(D) = P_1/P_2. \tag{11}$$

We use $D(\rho_p)$, which is the inverse function of $\rho_p(D)$ to determine the accurate position of the target. As shown in Fig. 2, accurate distance $R(t, v_{dn})$ is estimated by addition of $R_1(t, v_{dn})$ and the fractional range $D(\rho_p)$ as follows:

$$R(t, v_{dn}) = R_1(t, v_{dn}) + D(\rho_p). \tag{12}$$

With $R(t, v_{dn})$, $\theta_{AZ}(t, v_{dn})$ and $\theta_{EL}(t, v_{dn})$, the orbits of the scattering centers $\mathbf{x}_s(t, v_{dn})$ are determined by:

$$\mathbf{x}_s(t, v_{dn}) =$$
$$\begin{bmatrix} x_s(t, v_{dn}) \\ y_s(t, v_{dn}) \\ z_s(t, v_{dn}) \end{bmatrix} = \begin{bmatrix} R(t, v_{dn}) \cos\theta_{EL}(t, v_{dn}) \sin\theta_{AZ}(t, v_{dn}) \\ R(t, v_{dn}) \cos\theta_{EL}(t, v_{dn}) \cos\theta_{AZ}(t, v_{dn}) \\ R(t, v_{dn}) \sin\theta_{EL}(t, v_{dn}) + z_c \end{bmatrix}. \tag{13}$$

4. Experimental Setup and Examples

In this section we conduct an experiment using a human target to investigate the operation of the basic UWB Doppler radar interferometric imaging algorithm. Figure 3 shows the experimental site. We assume a pedestrian target on a treadmill with a belt speed of 3 km/h. In this experiment, the distance between the antennas and the target's torso is fixed to 2.7 m by using the treadmill to clarify the characteristics and problems of the basic UWB Doppler radar interferometric imaging algorithm. The heights of the pedestrian and the treadmill are 182 and 14 cm.

The center frequency of the transmitting pulse is f_0=26.4 GHz. Our experiment uses a CW signal modulated with an m-sequence of chip width 2 nsec, which gives the range resolution of ΔR=30 cm [20], [21]. The received signal waveform $s_{ik}(t)$ is acquired by taking a cross-correlation of a raw received signal with a time-shifted m-sequence [20]. Horn antennas are used with −3 dB beamwidth of ± 11° in both the E- and H-planes. The antenna separation d is set by consideration of aliasing and accuracy in the DOA estimation process. As shown in Eqs. (8) and (9), DOA estimation accuracy is improved by setting a large d. However, an unambiguous range of DOA is determined by d because of the aliasing. From Eq. (8), the unambiguous range of the elevation DOA is $\pm \sin^{-1}(\lambda/2d)$. Consequently, we must choose as large a d as possible, taking the observation area into consideration. Our experiments set d = 3.5 cm, and the unambiguous ranges of elevation and azimuth DOAs are both ±9.47°. These unambiguous ranges are sufficient for our experimental setting. The inter pulse period is 1.29 ms, and the window size w_T for SDFT is 165 ms. We take measurements at three antenna positions for the acquisition of data that correspond to the whole body: z_c=0.56, 1.26, and 1.81 m. Figure 4 shows the outline of the relationship between the target and the illumination area of the transmission beam at each antenna position. The antennas receive the echoes mainly from the head in position (i), arms and body in position (ii), and legs in position (iii).

Figure 5 shows a spectrogram at the range bin 9 (2.7 m) $|S_{19}(t, v_d)|^2$ for each antenna position. The radial velocity variations of the arms and legs are detected at antenna positions (ii) and (iii), and oscillations of the head and the body are observed at positions (i) and (ii). Figure 6 shows the human image estimated by the basic UWB Doppler radar interferometric imaging algorithm. Here, we use the data of half
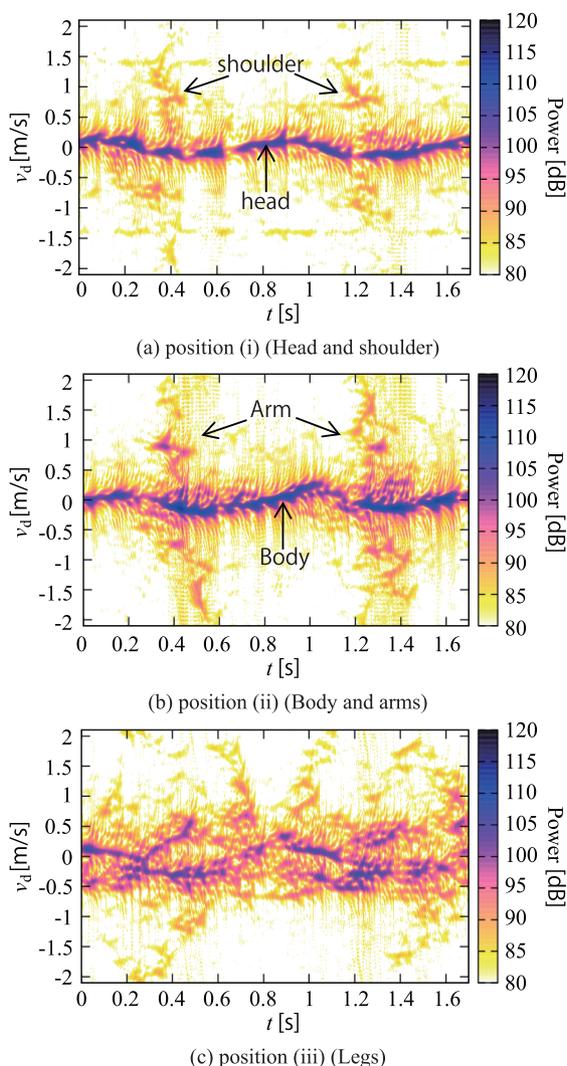
(a) position (i) (Head and shoulder)

(b) position (ii) (Body and arms)

(c) position (iii) (Legs)

Fig. 5 Spectrogram $|S_{19}(t, v_d)|^2$ in each antenna position.
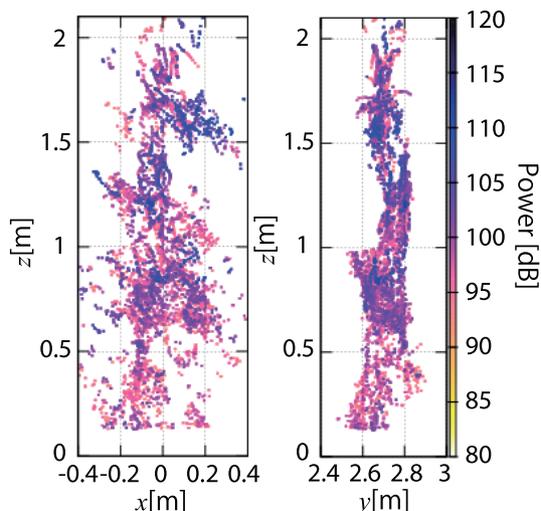

Fig. 6 Frontal (l) and side views (r) of image estimated by basic UWB Doppler radar interferometry.

a walking cycle for imaging, and set $\rho=0.25$. Since many false images are confirmed, we cannot accurately reconstruct the image of the human body from this result. These false images are caused by the interference of the echoes from various body parts.

5. False Image Detection and Rejection Method

5.1 False Image Rejection Method Using Velocity Information

To resolve the problem described in the previous section, we propose a false image detection and rejection method. First, we clarify the mechanism of such false images with a simple numerical simulation. We assume a two-point target that has a pendulum motion, and set the antenna separation $d=5$ mm and the center position of the antennas $z_c=0$. With this antenna setting, the unambiguous range of DOA is $\pm\pi/2$. Figure 7 shows the orbits of the targets. Omni-directional antennas are assumed, and the received signals are calculated with ray-tracing. Other radar settings and parameters are the same as in the previous section. Figures 8 and 9 show the spectrogram and the estimated image. The false images are estimated where the target does not exist. Comparing Figs. 8 and 9(b), we find that false images are generated when interference of the echoes has occurred. The DOA is estimated using the phase difference between two antennas, as expressed in Eqs. (8) and (9); however, the phase estimation errors are caused by interference. Figure 10(a) shows the outline of the phase estimation error at an antenna, where the horizontal and vertical axes are the real and imaginary parts of a received echo. Since this error is caused at all antennas, the estimated phase differences also have errors. For this reason, the DOA is estimated in the direction where the target does not exist. In addition, amplitude variation of the echo leads to fast motion of the false images. Figure 10(b) shows the effect on the amplitude variation and the phase error that occurred owing to the amplitude variation. For example, in Fig. 8, the amplitude ratio of targets 1 and 2 varies from 1.26 to 1.45 in 0.2 s $< t < 0.3$ s, and scattering centers corresponding to these data move at a velocity of approximately 4 m/s. This velocity is greater than the maximum velocity of the assumed target, which is 2.5 m/s.
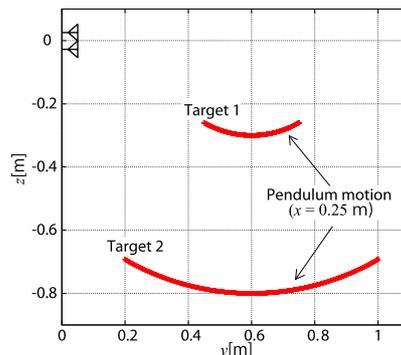

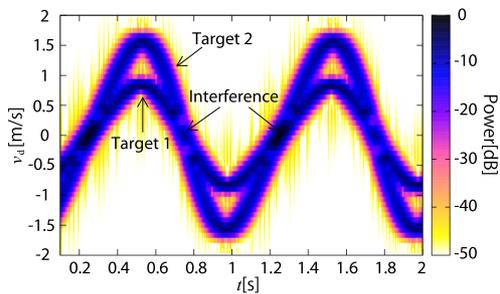**Fig. 7** Orbit of targets in numerical simulation.

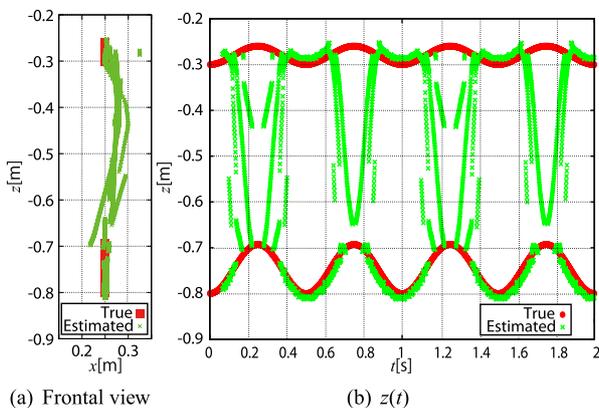**Fig. 8** Acquired spectrogram in simulation.

(a) Frontal view   (b) $z(t)$

Fig. 9 Estimated image in simulation.

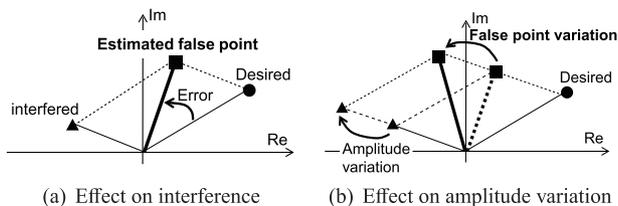(a) Effect on interference   (b) Effect on amplitude variation

Fig. 10 Outline of mechanism of false images.

Therefore, many false images have a velocity greater than the maximum velocity assumed by the motion type.

Based on the above discussion, we propose a false image rejection method. First, we reject the estimated points with relatively large velocities and remove the images that satisfy the following condition:

$$v_{max} < |\mathbf{v}(t, v_d)|, \tag{14}$$

where v_{max} is the assumed maximum speed, and $\mathbf{v}(t, v_d)$ is the velocity estimated as the time-derivative of a scattering center position as:

$$\mathbf{v}(t, v_d) = d\mathbf{x}_s(t, v_d)/dt. \tag{15}$$

Next, isolated points are removed. We assume a sphere with radius R_F whose center is at $\mathbf{x}_s(t, v_{dn})$, and count the number of scattering centers N_F within it. We reject the scattering centers that satisfy the condition:

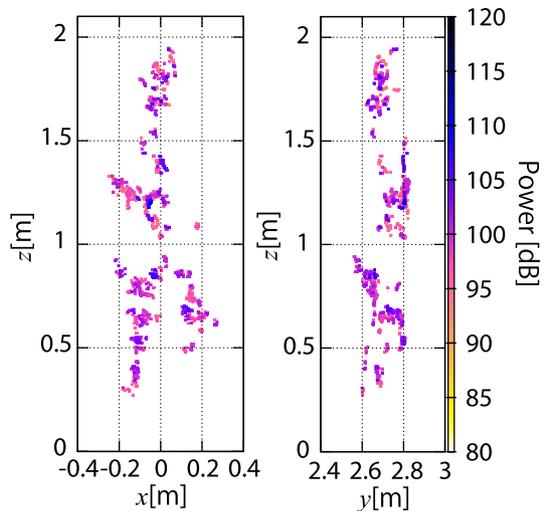$$N_F/N_A < \alpha, \tag{16}$$

Fig. 11 Frontal (l) and side views (r) of estimated image after applying the false image rejection method.

where N_A is the total number of estimated points, and $\alpha < 1$ is the threshold ratio of the number of false points to the total number of points. α is empirically determined by the spatial resolution.

Figure 11 shows the estimated image after applying the false image reduction method to the same data as in Fig. 6. We empirically set v_{max}=2.5 m/s, $R_F = \Delta R/10 = 3$ cm, and α=0.003. The proposed method removes most of the false images. However, the estimated region becomes small, because weak echoes from some body parts are also suppressed by this simple false image reduction method. For example, the echo intensity from the arms is lower than that from a torso as shown in Fig. 5(b).

5.2 Adaptive Peak Extraction

For detection of low power echoes, relatively low ρ must be set in Eq. (7). However, false peaks caused by interference are not suppressed when threshold ρ is small. Figures 12(a) and (b) shows examples of echo peaks estimated for $\rho = 0.25$ and 0.15. Here, the false image rejection method described in the previous section is applied. As illustrated in these examples, the number of extracted peaks corresponding to the arms is relatively small for $\rho = 0.25$, and many false peaks remained for $\rho = 0.15$. This is because the threshold that we used was fixed independently of v_d. To resolve this problem, we modified the Eq. (7):

$$|S_{ij}(t, v_d)|^2 > \rho(v_d) \max_{v_d} |S_{ij}(t, v_d)|^2. \tag{17}$$

This condition means that threshold ρ depends on v_d. In walking motion, for example, the swinging motion of the arm has large radial velocity compared with the body oscillation. Thus, if v_d is large, $\rho(v_d)$ should be small in position (ii).

We next explain how to determine the threshold $\rho(v_d)$. As discussed above, $\rho(v_d)$ should be changed depending
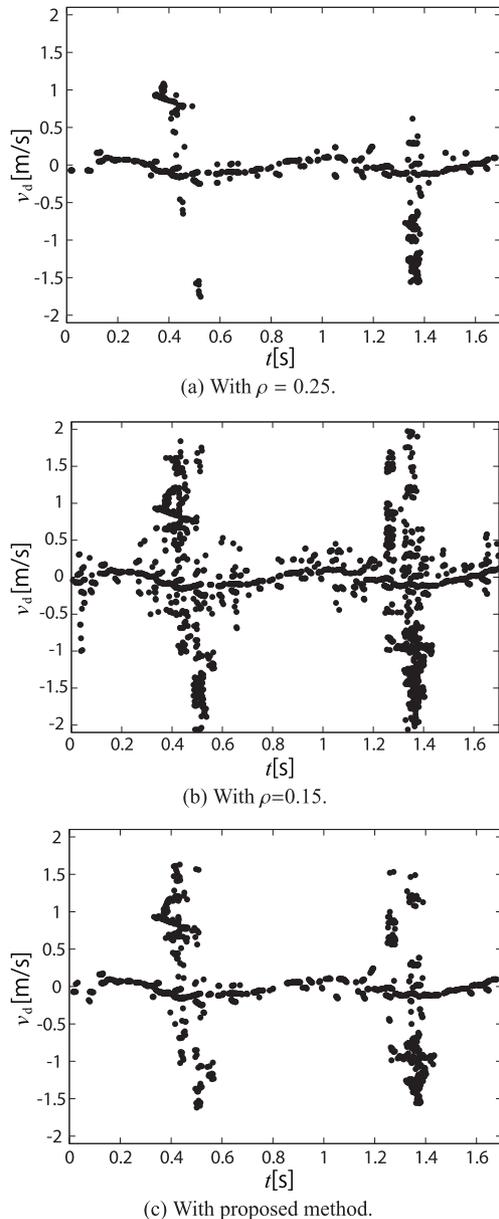
(a) With $\rho = 0.25$.

(b) With $\rho = 0.15$.

(c) With proposed method.

Fig. 12　Extracted peaks from spectrogram in position (ii).

Fig. 13　Procedure of proposed imaging algorithm.

3. Count the number of points N_{Ik} satisfying Eqs. (14) and (16).
4. Estimate $\beta_k = N_{Ik}/N_{Ak}$, where N_{Ak} is the total number of estimated points.
5. If $\beta_k < \beta_{th}$ or $N_{Ak} = 0$, determine $\rho(k\Delta v_d) \leftarrow \rho_k$. Otherwise, $\rho_k \leftarrow \rho_k + \Delta\rho$ and go to 2.

Figure 12(c) shows the peaks extracted using the proposed extraction method. We empirically set $N_v = 16$, $\beta_{th} = 0.6$, $\gamma = 1/10000$ and $\Delta\rho = 0.01$. This figure indicates that peaks corresponding to both the body and the arms are accurately extracted. Moreover, the number of false peaks is reduced compared with the image in Fig. 12(b) for a fixed-threshold $\rho = 0.15$.

The procedure of the proposed imaging algorithm is summarized in Fig. 13. Our proposed imaging algorithm generates images using the basic UWB Doppler interferometric imaging algorithm and extracts reliable images using the methods described in Sects. 5.1 and 5.2.

6. Results and Discussion

6.1 Human Imaging Results and Performance

Figure 14 shows the estimated image after applying the adaptive peak extraction method to the data of Fig. 11. The estimated region becomes large without increasing the false images, and an outline of the human body is estimated. In addition, the proposed imaging algorithm also acquires the radial velocity of each estimated scattering center. Figure 15(a) shows the radial velocity of Fig. 14. This figure indicates that radial velocities corresponding to the walking motion were detected. From the data of Fig. 14, when the right foot swings forward, the positive radial velocity corresponding to this motion is observed, and the left foot has negative radial velocity. In addition, Fig. 15(b) shows the image estimated from the data of the next half of a walking cycle of Fig. 15(a). The signs of the radial velocities of the

on the echo power. In addition, false echo peaks are not suppressed by the false image rejection method when ρ is set to be small. Consequently, if the amount of interference is relatively large, $\rho(v_d)$ should be set to a large value. We divide the radial velocity axis between N_v segments: $v_{dmax} - (k-1)\Delta v_d$-$v_{dmax} - k\Delta v_d$ ($k = 1, 2, \cdots, N_v$), where $\Delta v_d = 2v_{dmax}/N_v$ and v_{dmax} is the maximum radial velocity. The threshold for each segment k is defined as $\rho(k\Delta v_d)$. For each segment k, the following procedures determine $\rho(k\Delta v_d)$:

1. Estimate the maximum power density $P_{max k}$ and noise power density P_{Nk}, and set $\rho_k = \gamma P_{max k}/P_{Nk}$.
2. Extract the peaks satisfying Eq. (17) for $\rho(k\Delta v_d) = \rho_k$ and obtain an image.
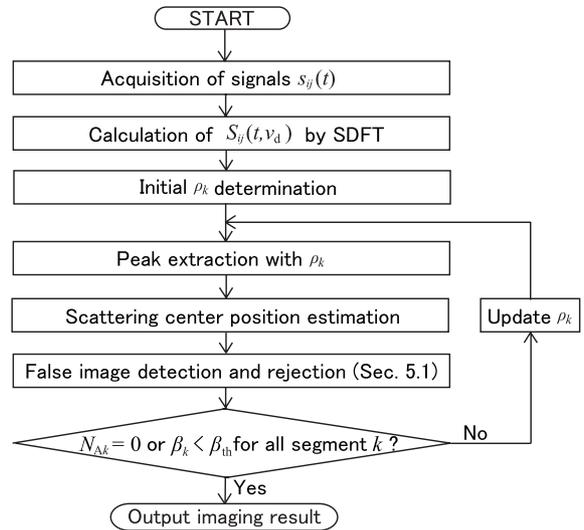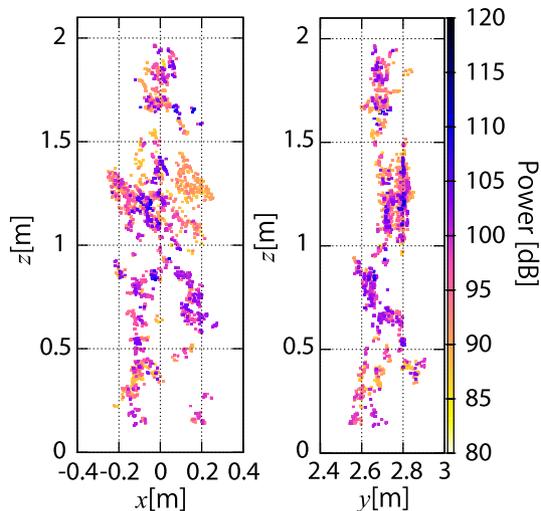
Fig. 14 Frontal (l) and side views (r) of estimated image using the proposed imaging algorithm.

(a) With data of Fig. 14

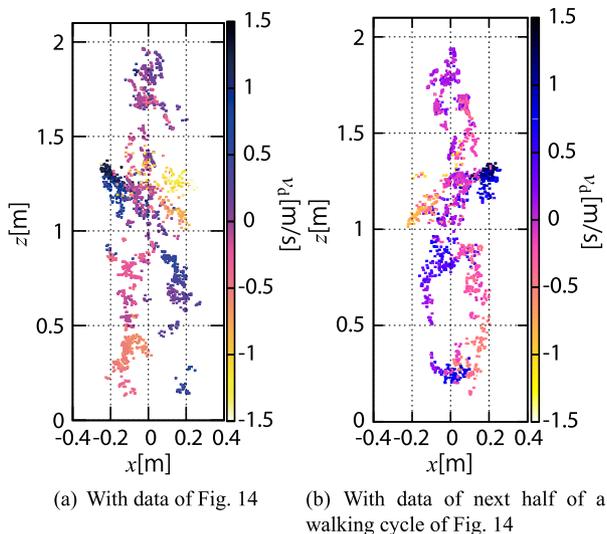(b) With data of next half of a walking cycle of Fig. 14

Fig. 15 Radial velocity of each estimated point.

legs and arms are reversed compared with Fig. 15(a). This important pedestrian feature is observed.

Next, we investigate the accuracy of the estimated image from its side view. We compare the scattering center positions extracted from the video and the image estimated by the proposed imaging algorithm. A scattering center is the position where a radar radial direction and a target surface intersect perpendicularly. We calculate such points from the video. Figure 16 shows the scattering center position extracted from the video and estimated side views in positions (ii) and (iii). Although many estimated scattering centers are matched, some imaging points are estimated where scattering centers are not obtained from the video. In Fig. 16(b), the extraction of the scattering centers corresponding to shoes from the video is difficult. Thus, we might think that the imaging points near (y, z)=(2.85 m, 0.4 m) and (2.7 m, 0.35 m) correspond to the shoes. Simi-

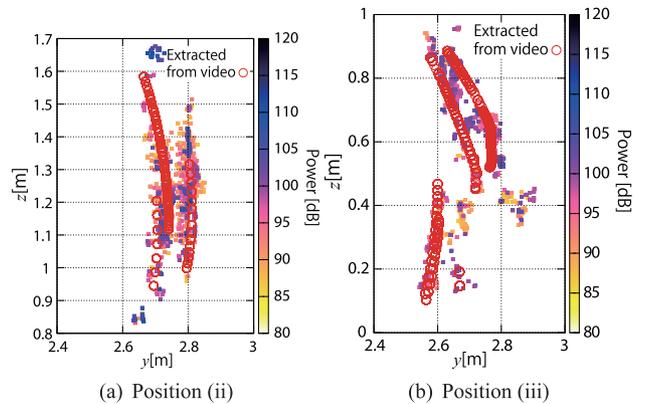(a) Position (ii)

(b) Position (iii)

Fig. 16 Estimated points and scattering centers extracted from the video in side view.

larly, in Fig. 16(a), strict scattering center estimation from the body is difficult. However, we can confirm that many scattering centers are accurately estimated except for such points. These results verify that the proposed imaging algorithm achieves adequate human imaging in a real environment and can acquire features of the image motion.

6.2 Shape/Motion Parameter Extraction

This subsection describes shape/motion parameter extraction examples. We extract these parameters: walking cycle, step, shoulder width, and height. A walking cycle corresponds to two spectrogram cycles. Hence we estimate the cycle of the spectrogram T_s using the Fourier transform, and then the walking cycle is estimated as $T_w = 2T_s$. Next, a walking step is estimated from T_w and the walking velocity. The walking velocity is estimated by deriving it from the scattering centers of the body. However, this study assumes a pedestrian on a treadmill; therefore the walking velocity v_w is the treadmill's belt speed. Walking step A_w is estimated by:

$$A_w = \frac{v_w T_w}{2}. \tag{18}$$

Shoulder width and height are directly estimated from a frontal view of the human image. The maximum and minimum values of the estimated image in terms of the x axis are x_{max} and x_{min}. Shoulder width L_s is estimated by:

$$L_s = x_{max} - x_{min}. \tag{19}$$

In the same way, height L_h is estimated by:

$$L_h = z_{max} - z_{min}. \tag{20}$$

Table 1 shows the true and estimated parameters of a pedestrian target of Fig. 3. We use the same data as in Fig. 15. This table shows that all parameters were accurately extracted.
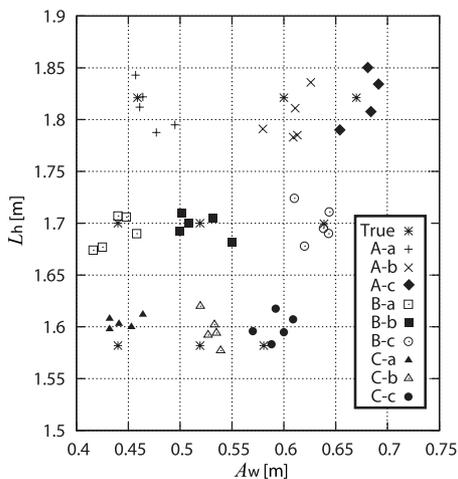
Next, we demonstrate the parameter extraction for a variety of pedestrians. Table 2 shows the assumed targets and their heights and steps. We assume three pedestrian subjects

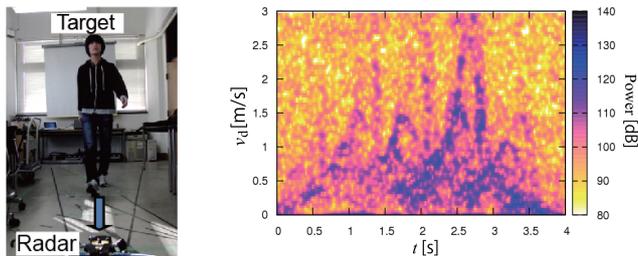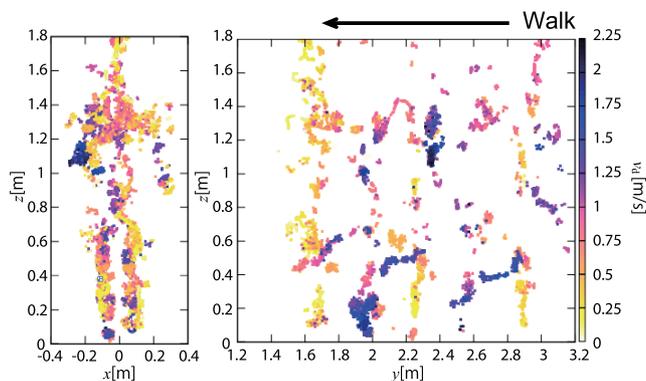**Table 1** True and estimated parameters for target of Fig. 3.

Parameter	True	Estimated
Walking cycle T_w	1.44 s	1.50 s
Step A_w	60.0 cm	62.5 cm
Shoulder length L_s	46.0 cm	49.4 cm
Height L_h	182 cm	184 cm

Table 2 Assumed targets for the experiment of shape/motion parameter extraction, and their true heights and steps.

	Target A	Target B	Target C
Height	182 cm	170 cm	158 cm
Step a (small)	46 cm	44 cm	44 cm
Step b (middle)	60 cm	52 cm	52 cm
Step c (large)	67 cm	64 cm	58 cm

Fig. 17 Relationship between extracted A_w and L_h of each target.

whose heights are different. Each pedestrian walks with three types of steps on the treadmill. We identify nine types of targets by extracted height L_h and step A_w and measure them sequentially. The experimental setting and parameters are the same as in the previous section. Figure 17 shows the relationship between the extracted A_w and L_h. In this figure, we used the data of a walking cycle to estimate A_w and L_h, and plot the parameters of five walking cycles for each target. We realized accurate parameter extraction, and it is easy to confirm that nine types of data were used. The mean errors of A_w and L_h are 1.45 cm and 4.17 cm. These results verify that accurate extraction of walking parameters is achieved from the human image estimated by the proposed imaging algorithm.

(a) Experimental site (b) Summation of the spectrograms for range bins

Fig. 18 Experimental setup and spectrogram at $z_c = 0.36$vm of a pedestrian target without a treadmill.

Fig. 19 Frontal (l) and side views (r) of estimated image of an pedestrian walking toward the radar without a treadmill.

6.3 Application to a Pedestrian Target Walking Toward the Antennas

In this subsection, we assume an actual pedestrian target without a treadmill, and clarify the performance of the proposed imaging algorithm in a realistic situation. Figure 18(a) shows the experimental site. The target walks from $(x, y) = (0, 3.9$ m$)$ to $(0, 1.5$ m$)$ with a walking step of 0.6 m and a mean speed of 0.86 m/s. The height of the examinee is 1.75 m. We measure at four antenna positions: z_c=0.36, 0.82, 1.29, and 1.54 m. We measured data at not three but four different positions in this case because three antenna positions cannot cover the whole body when the target is close to the radar system. Figure 18(b) shows the summation of the spectrograms for all range bins at $z_c = 0.36$ m. The radial velocity variations of his legs are confirmed, and the offset of the spectrograms corresponds to the mean walking speed.

Figure 19 shows the image estimated by the proposed algorithm using the data of $t \geq 1.5$ s. This is because that the signal-to-noise ratio at $t < 1.5$ s is insufficient for an imaging. Parameters v_{max}, R_F, and α have the same values as in the previous subsection. We extract the outline of the human and the radial velocity features of the walking motion. With the side view, we can see the walking motion which corresponds to three steps. Note that our imaging capability only depends on a signal-to-noise ratio, not the distance
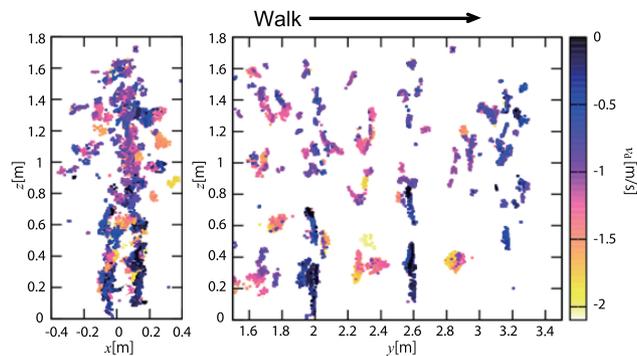
Fig. 20 Frontal (l) and side views (r) of estimated image of a pedestrian who walks away from the radar along the y-axis.

Fig. 21 Top (l) and frontal views (r) of estimated image of a pedestrian with an oblique walking direction (case A).

Fig. 22 Top (l) and frontal views (r) of estimated image of a pedestrian with an oblique walking direction (case B).

between the target and the antennas. In $z < 0.8$ m, the scattering centers with relatively large velocities corresponds to the swinging of the leg, and the scattering centers with small v_d corresponds to the other leg in contact with the ground. Moreover, the arm swinging motion is detected as relatively large velocities over about 0.8 m $< z <$ 1.3 m. These results mean that we can confirm the walking motion features, and the effectiveness of our proposed algorithm is also confirmed for an actual pedestrian target without a treadmill.

6.4 Imaging Examples of a Pedestrians Moving in Various Directions

This subsection shows imaging examples of pedestrian targets having a variety of directions. The parameters of the radar and the proposed algorithm are the same as in the previous section. First, we assume a pedestrian who walks away from the radar. The target walks from (x, y)=(0 m, 1.5 m) to (0 m, 3.9 m) with a walking step of 0.6 m and a mean speed of 0.86 m/s. The height of the examinee is 1.63 m. Figure 20 shows the frontal and side views of the estimated image using the data with sufficient signal-to-noise ratio. This figure confirms that the human outline and the features of walking motion are obtained same as the example described in the previous section.

Finally, we show the imaging results of pedestrians having oblique walking directions. We assume two scenarios: case A assumes the target walks from (x, y)=(−1.03 m, 2.69 m) to (1.03 m, 1.51 m) and case B assumes the target walks from (x, y)=(−1.03 m, 2.41 m) to (1.03 m, 1.79 m). In both scenarios, the mean speed and the height of the target are 0.8 m/s and 1.78 m. Figure 21 shows the top and frontal views of the estimated image for case A, where X is the axis perpendicular to the walking direction. We use the data which corresponds to the target within the beam illumination area. Although the number of scattering centers in the relatively large X is small because of shadowing, a human outline and walking orbit are sufficiently detected. Figure 22 shows the top and frontal views of the estimated image for case B. The radial velocities become small compared with case A because the walking orbit is close to cross-range direction. In addition, the effect on the shadowing is larger
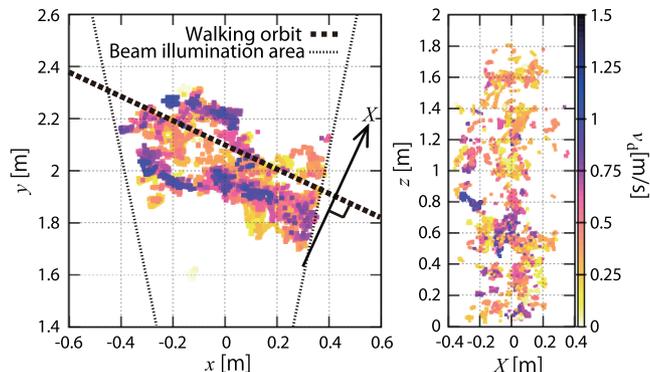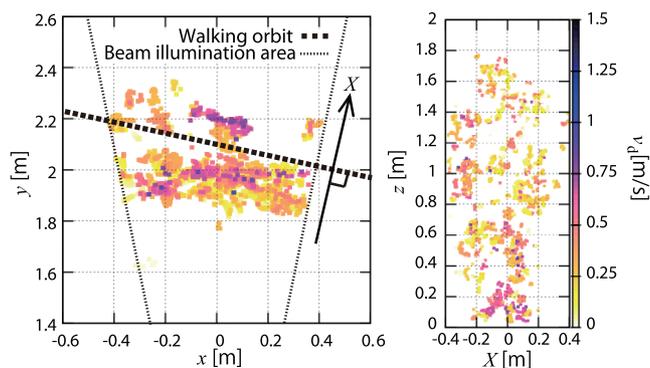
than case A. However, the walking orbit and the human outline are extracted to some extent. These results indicate that our proposed method is applicable to target motion with arbitrary directions.

7. Conclusions

This study proposed a human imaging algorithm with UWB Doppler radar. We explained the operation of the basic UWB Doppler radar interferometric imaging algorithm and showed that its use yields many false images because of interference. We then clarified the mechanism of such false images, and proposed false image detection and rejection methods using velocity information. The experiment, which assumed a pedestrian on a treadmill, indicated that the proposed imaging algorithm achieved adequate human imaging. Walking motion features were also confirmed. We also examined shape and motion parameter extraction, and verified that accurate parameters can be extracted from the estimated human images. Finally, we conducted experiments that assumed an actual pedestrian target without a treadmill. These experiments verified that our proposed imaging algorithm achieved estimation of a human outline and a walking orbit for the pedestrian targets walking in various directions.

Acknowledgments

References

[1] M. Elbouz, A. Alfalou, and C. Brosseau, "Fuzzy logic and optical correlation-based face recognition method for patient monitoring application in home video surveillance," Optical Engineering, vol.50, no.6, Article Number 067003, 2011.

[2] S.C. Hsia, C.H. Hsiao, and C.Y. Huang, "Single-object-based segmentation and coding technique for video surveillance system," J. Elec. Imag., vol.18, no.3, Article Number 033007, 2009.

[3] S. Nobuhara, Y. Tsuda, I. Ohama, and T. Matsuyama, "Multi-viewpoint silhouette extraction with 3D context-aware error detection, correction, and shadow suppression," IPSJ Trans. Comp. Vis., vol.1, pp.242–259, 2009.

[4] A. Mittal and L.S. Davis, "A general method for sensor planning in multi-sensor systems: Extension to random occlusion," Int. J. Comput. Vis., vol.76, no.1, pp.31–52, 2008.

[5] G. Vogiatzis, C. Hernandez, P.H. S. Torr, and R. Cipolla, "Multi-view stereo via volumetric graph-cuts and occlusion robust photo-consistency," IEEE Trans. Pattern Anal. Mach. Intell., vol.29, no.12, pp.2241–2255, 2007.

[6] S. Ikeda, H. Tsuji, and T. Ohtsuki, "Indoor event detection with signal subspace spanned by eigenvector for home or office security," IEICE Trans. Commun., vol.E92-B, no.7, pp.2406–2412, July 2009.

[7] A.O. Salman, D. Dibekci, S.P. Gavrilov, and A.A. Vertiy, "The radiation properties of a novel wire antenna for the security fence radar," IEEE Trans. Antennas Propag., vol.56, no.9, pp.2852–2864, 2008.

[8] K. Inomata, T. Hirai, Y. Yamaguchi, and H. Yamada, "Two-dimensional target location estimation technique using leaky coaxial cables," IEICE Trans. Commun., vol.E91-B, no.3, pp.878–886, March 2008.

[9] E. Paolini, A. Giorgetti, M. Chiani, R. Minutolo, and M. Montanari, "Localization capability of cooperative anti-intruder radar systems," EURASIP J. Adv. Sig. Proc., Article Number 726854, 2008.

[10] K. Suwa, T. Wakayama, and M. Iwamoto, "Three-dimensional target geometry and target motion estimation method using multistatic ISAR movies and its performance," IEEE Geosci. Remote Sens., vol.49, no.6, pp.2361–2372, 2011.

[11] X. Lv, M. Xing, C. Wan, and S.Z. Li, "ISAR imaging of maneuvering targets based on the range centroid Doppler technique," IEEE Trans. Image Process., vol.19, no.1, pp.141–153, 2010.

[12] T. Sakamoto and T. Sato, "A target shape estimation algorithm for pulse radar systems based on boundary scattering transform," IEICE Trans. Commun., vol.E87-B, no.5, pp.1357–1365, May 2004.

[13] T. Sakamoto and T. Sato, "2-Dimensional imaging of human bodies with UWB radar using approximately uniform walking motion along a straight line with the SEABED algorithm," IEICE Trans. Commun., vol.E91-B, no.11, pp.3695–3703, Nov. 2008.

[14] Y. Matsuki, T. Sakamoto, and T. Sato, "An imaging algorithm of a target with arbitrary motion for ultra wide-band radar with a small number of antennas," IEICE Trans. Commun., vol.E94-B, no.3, pp.742–749, March 2011.

[15] A. Lin and H. Ling, "Doppler and direction-of-arrival (DDOA) radar for multiple-mover sensing," IEEE Trans. Aerosp. Electron. Syst., vol.43, no.4, pp.1496–1509, 2007.

[16] A. Lin and H. Ling, "Frontal imaging of human using three element Doppler and direction-of-arrival radar," Electron. Lett., vol.42, no.11, pp.660–661, 2006.

[17] A. Lin and H. Ling, "Three-dimensional tracking of humans using very low complexity radar," Electron. Lett., vol.42, no.18, pp.1062–1063, 2006.

[18] Y. Kim and H. Ling, "Human activity classification based on micro-Doppler signatures using a support vector machine," IEEE Trans. Geosci. Remote Sens., vol.47, no.5, pp.1328–1337, 2009.

[19] E. Jacobsen and R. Lyons, "The sliding DFT," IEEE Trans. Signal Process. Mag., vol.20, no.2, pp.74–80, 2003.

[20] R. Pickholts, D. Schilling, and L.B. Milstein, "Theory of spread-spectrum communications-A tutorial," IEEE Trans. Commun., vol.COM-30, no.5, pp.855–882, 1982.

[21] T. Fukuda, N. Nagoro, S. Ujita, S. Nagai, M. Nishijima, H. Sakai, T. Tanaka, and D. Ueda, "A 26 GHz short-range UWB vehicular radar using 2.5 Gcps spread spectrum modulation," Microwave Symposium, 2007. IEEE/MTT-S International, pp.1311–1314, 2007.

Kenshi Saho received his B.E. degree from Kyoto University in 2008 and M.I. degree from Graduate School of Informatics, Kyoto University in 2010. He is currently a research fellow of the Japan Society for the Promotion of Science (JSPS), studying toward his Ph.D. degree at the Graduate School of Informatics, Kyoto University. His current research interest is in UWB radar signal processing. He is a student member of the IEEJ.

Takuya Sakamoto received his B.E. degree from Kyoto University in 2000, and M.I. and Ph.D. degrees from the Graduate School of Informatics, Kyoto University in 2002 and 2005, respectively. He is an assistant professor in the Department of Communications and Computer Engineering, Graduate School of Informatics, Kyoto University. His current research interest is in UWB radar signal processing. He is a member of the IEEJ and the IEEE.

Toru Sato received his B.E., M.E., and Ph.D. degrees in electrical engineering from Kyoto University, Kyoto, Japan in 1976, 1978, and 1982, respectively. He has been with Kyoto University since 1983 and is currently a Professor in the Department of Communications and Computer Engineering, Graduate School of Informatics. His major research interests include system design and signal processing aspects of UWB radars, atmospheric radars, radar remote sensing of the atmosphere, and radar observation of space debris. He is a member of the Institute of Electrical and Electronics Engineers, the Society of Geomagnetism and Earth, Planetary and Space Sciences, the Japan Society for Aeronautical and Space Sciences, and American Meteorological Society.

Kenichi Inoue received the B.S. and M.S. degrees in electronic science and engineering from Kyoto University, Kyoto, Japan, in 2000 and 2002, respectively. In 2002, he joined Semiconductor Device Research Center, Semiconductor Company, Matsushita Electric Industrial Co. Ltd., Osaka, Japan, where he was working on semiconductor laser devices, sensor devices and sensor systems. Since 2009, he has been with Advanced Technology Research Laboratories, Panasonic Corporation, Kyoto, Japan, where he is involved in the research and development of UWB radar sensor system and its applications. Mr. Inoue is a member of the Japan Society of Applied Physics.

Takeshi Fukuda was born in Osaka, Japan, in 1969. He received the B.S. and M.S. degrees in Electronic Engineering from Osaka University, Suita, Japan, in 1993 and 1995, respectively. In 1995, he joined the Electronics Research Laboratory, Matsushita Electronics Corporation, Osaka, Japan, where he has been engaged in the research and development of microwave integrated circuits. Since 2009, he has been with Advanced Technology Research Laboratories, Panasonic Corporation, Kyoto, Japan. His current research interests are algorithms and RF architectures for high-resolution millimeter-wave radar systems.